

Simulation of finite-size fibers in turbulent channel flows

M. Do-Quang,^{*} G. Amberg, G. Brethouwer, and A. V. Johansson

Linné FLOW Center, Mechanics Department, Royal Institute of Technology, SE-100 44, Stockholm, Sweden

(Received 22 May 2013; revised manuscript received 7 October 2013; published 9 January 2014)

The dynamical behavior of almost neutrally buoyant finite-size rigid fibers or rods in turbulent channel flow is studied by direct numerical simulations. The time evolution of the fiber orientation and translational and rotational motions in a statistically steady channel flow is obtained for three different fiber lengths. The turbulent flow is modeled by an entropy lattice Boltzmann method, and the interaction between fibers and carrier fluid is modeled through an external boundary force method. Direct contact and lubrication force models for fiber-fiber interactions and fiber-wall interaction are taken into account to allow for a full four-way interaction. The density ratio is chosen to mimic cellulose fibers in water. It is shown that the finite size leads to fiber-turbulence interactions that are significantly different from earlier reported results for pointlike particles (e.g., elongated ellipsoids smaller than the Kolmogorov scale). An effect that becomes increasingly accentuated with fiber length is an accumulation in high-speed regions near the wall, resulting in a mean fiber velocity that is higher than the mean fluid velocity. The simulation results indicate that the finite-size fibers tend to stay in the high-speed streaks due to collisions with the wall. In the central region of the channel, long fibers tend to align in the spanwise direction. Closer to the wall the long fibers instead tend to toward to a rotation in the shear plane, while very close to the wall they become predominantly aligned in the streamwise direction.

DOI: [10.1103/PhysRevE.89.013006](https://doi.org/10.1103/PhysRevE.89.013006)

PACS number(s): 47.27.nd, 47.85.-g, 47.57.E-

I. INTRODUCTION

Fiber suspension flows are found in many scientific and engineering applications, prime examples being the pulp and paper industry. Even though paper making is an ancient process and has much evolved over the centuries, it is still resource and energy intensive with clear potential for improvements [1]. The flow physics of cellulose fiber suspensions has an important impact on many steps of the paper-making process while the distribution and orientation of the fibers, which depend on the interaction between the fibers and the flow and fiber-fiber interactions, determine the properties of the final paper.

The motion of nonspherical particles, e.g., ellipsoids, in simple nonturbulent shear flows has been studied intensively [2] derived analytic expressions for the rotation of inertialess ellipsoids in Stokes shear flow, while in recent studies the effects of fluid and/or particle inertia on the motion of nonspherical particles in shear flows were considered [3–5]. Depending on the particle shape and the inertia of fluid and particle, different motions are possible, for example, tumbling (periodic rotations in the shear plane with a nonconstant speed), wagging (oscillations with the fiber approximately aligned with the flow), kayaking (motions about the vorticity axis resembling paddling), log-rolling (rolling of a fiber aligned with the vorticity axis), and even chaotic motions with no discernible pattern [5]. Here and hereafter we use the same naming convention for fiber motions as in Ref. [6]. Krochak *et al.* [7] modeled the distribution and orientation of a semidilute fiber suspension in laminar channel flow taking into account the fiber-fiber and the fiber-wall interactions and found good agreement with experimental observations. At low concentrations, the fibers are mostly parallel to the flow near the wall, and the fiber concentration has its maximum at the channel center since the fibers tend to migrate away from the wall.

Fiber suspensions in turbulent flows have also been investigated. Zhang *et al.* [8] studied the transport and deposition of ellipsoids in turbulent channel flow through direct numerical simulations (DNS). More recently, Mortensen *et al.* [9] and Marchioli *et al.* [10] carried out DNS of fully developed turbulent channel flow at $Re_\tau = u_\tau h/\nu = 180$ and 150, respectively, with spherical to very elongated prolate ellipsoids with different inertia. Here u_τ is the friction velocity, h the channel half-gap, and ν the kinematic viscosity of the fluid phase. In those studies, the particles were assumed to be smaller than the Kolmogorov length scale, and gravity, fiber-fiber interactions, and the fiber influence on the flow were ignored. Under these circumstances, the particles could be treated as point particles with the same equations of motion as that of an ellipsoid in creeping flow. Furthermore, the particles were assumed to keep their streamwise linear and angular momentum when having elastic collisions with the wall.

Mortensen *et al.* observed that both spheres and ellipsoids are preferentially concentrated in the near-wall low-speed streaks. As a consequence, lighter particles were slower than the mean fluid velocity near the wall while the velocity of the heavier particles exceeded the mean fluid velocity in the viscous sublayer, but was lower than the mean fluid velocity in the buffer layer. Marchioli *et al.* found that the preferential concentration of the ellipsoids in the low-speed streaks is predominantly determined by their inertia. The aspect ratio of the particles had only a minor influence. In addition, particles showed a strong accumulation near the wall due to their inertia. For this aspect, the aspect ratio had some influence. Like Mortensen *et al.*, Marchioli *et al.* also studied the orientation of the ellipsoids or fibers and observed that the fibers tend to align with the mean flow near the wall while near the channel center their orientation is approximately isotropic.

Other investigations addressed the effect of small fibers and ellipsoids on turbulent wall-bounded flows and found that fibers can induce significant drag reduction [11–14] and typically enhance the streamwise component of the velocity

^{*}minh@mech.kth.se

fluctuations while damping the spanwise and wall-normal components.

Although our knowledge of fiber suspensions in turbulent flows is considerable, there are clear gaps. For instance, the effect of fiber size in turbulent flows is not well understood since most of the numerical studies so far considered only fibers (much) smaller than the Kolmogorov length scale. However, finite-size effects might have an important impact on the physics of fiber suspensions, since the dynamics of the interaction between fibers and turbulence should become significantly different when the length of the fibers becomes comparable to the size of the turbulent eddies. For instance, Kvick *et al.* [15] found in their experiments that the fiber length has a significant effect on the fiber orientation. Modern numerical methodologies make it possible to investigate flows with finite-size particles that are not necessarily small compared to the turbulence scales and to take full account of particle-flow interactions. Ten Cate *et al.* [16] used the body force term method to simulate finite-size spheres in isotropic turbulence, and [17] and Villalba *et al.* [18] simulated vertical turbulent channel flow with finite-size rigid particles using the immersed boundary method. The lattice Boltzmann method (LBM) is another, promising approach to simulate multiphase flows with finite-size particles [19,20].

The objective of this work is to examine the largely unknown influence of fiber size on the transport, distribution, and orientation of a dilute suspension of rigid fibers in fully developed turbulent channel flow. We will use LBM to simulate the fiber suspension flow. The largest fibers have a significant length compared to the near-wall turbulence structures, and their properties are similar to that of cellulose fibers in water. Fiber-flow interactions are accurately resolved, and fiber-fiber as well as fiber-wall interactions are taken into account in our study since the forces acting on the fibers when they have contact with the wall (or each other) can change the linear and angular momentum of the fibers and affect their distribution, orientation, and transport.

In the next part, an outline of the numerical methodology is given and the method is validated. Thereafter, the results of the simulations of fiber suspensions in turbulent channel flow are presented and analyzed and conclusions are drawn.

II. NUMERICAL METHOD

In this paper an entropic lattice-Boltzmann method for turbulent flow [21] (see Appendix C and D for details) is used along with the fluid-solid interaction (FSI) method [22,23]. A detailed description of the LBM-EBF method and validations for rigid fibers, flexible fibers and deformable objects was recently presented in Refs. [22,23]. The full derivation of the LBM-EBF method is presented in Appendices A–D.

The EBF method employs an external force term in the lattice Boltzmann equation to impose a no-slip boundary condition at the fluid-solid interface while conserving mass and momentum. To transfer the velocity and the force values between Eulerian grid positions and particle-related Lagrangian positions, we use the regularized delta function approach found in Ref. [24]; see Appendix A for more details.

In our model each fiber or rod is mapped onto a superimposed Lagrangian frame moving continuously throughout the

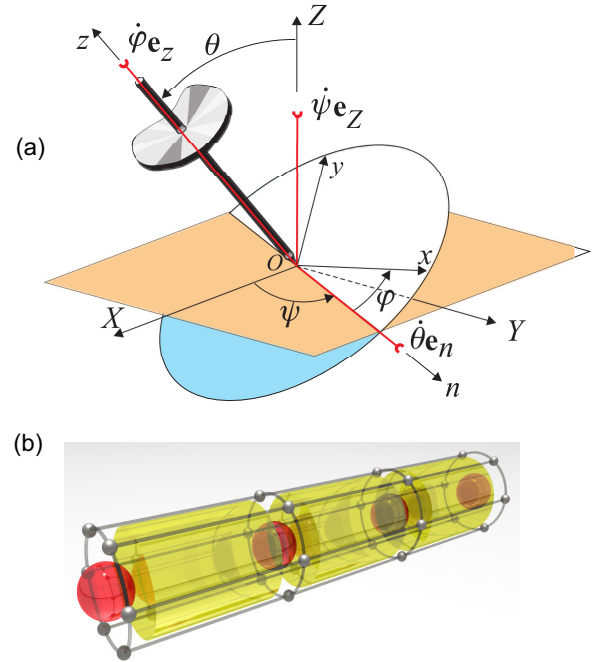


FIG. 1. (Color online) (a) The coordinate systems: a Cartesian coordinate system x - y - z for spatial parametrization (corresponding to streamwise, wall normal, and spanwise directions in channel flow) and a body-fixed coordinate system X - Y - Z for the fiber rotation. (b) The fiber is modeled as a chain of rods (yellow cylinders), which is connected via a hinge (red sphere), in this paper taken as rigid. The silver spheres are the Lagrangian grid points on the surface of the fiber. The aspect ratio of the Lagrangian grid used in this figure is for visualization only.

fluid domain. This means that when a fiber is transported out of the fluid domain, it will enter the domain at the opposite side. The orientation of each fiber can be described in Eulerian coordinates using a unit vector \mathbf{z} along the fiber axis, as depicted in Fig. 1(a). The angles φ , θ , and ψ define \mathbf{z} for each fiber. The motion and orientation of the fiber is determined by solving Newton's equations for linear and angular momentum with fluid-solid interaction forces determined by the EBF method; see Appendix A for details. Contact and lubrication force models for fiber-fiber interactions and fiber-wall interaction have also been implemented in our model; see Appendix B. As can be seen from Eq. (B1) in Appendix B, the lubrication force is a function of the fluid viscosity (μ) and of the relative velocity between the surfaces (\mathbf{V}_{app}) and the average normal vector of those surfaces (\mathbf{n}_{avg}). Therefore the direction and the magnitude of the interaction force will depend on the fluid viscosity, the orientation of the fiber, and its velocity. This model is a kind of an in-elastic collision model. If the fiber keeps moving closer to the wall and if the distance to the wall is less than σ_c we switch to use a repulsive force (\mathbf{F}_{con}) to prevent fibers from penetrating each other and penetrating the wall. The collision model is then assumed to be elastic.

The fiber model used in this paper is similar to the one proposed [25] for flexible fibers and expanded [26] to include particle inertia, hydrodynamic fiber-fiber interactions, and two-way coupling between fiber and fluid. Recently this model

has been used [22] in the framework of an external boundary force method. The fiber is modeled as a chain of rods and hinges; see Fig. 1(b). Each hinge uses N_n nodes on the circumference to calculate the solid-liquid interaction force. It is also possible to include bending, twisting, and elastic forces at each boundary node, but in this paper, these forces are not considered because the fiber is considered to be rigid. The dynamic motion of the fiber will be computed based on the total force acting on the hinges.

A. Validation of the model for nonspherical particle

To validate our numerical method, we first analyze the motion of a rigid rod in a simple shear flow at a low Reynolds number and compare it with the analytical expression derived [2] of a solid ellipsoid in a simple shear flow at zero Reynolds number.

Previous work [2] has showed that a single, neutrally buoyant, non-Brownian, inertialess ellipsoid in a simple shear flow rotates around the vorticity axis [z axis in Fig. 1(a)] with a periodic motion. The orbit is such that the quantity

$$C = \frac{\tan \theta}{a_r} \sqrt{a_r^2 \cos^2 \phi + \sin^2 \phi} \quad (1)$$

remains constant. Here a_r is the ratio of the two principal axes of the ellipsoid. For a circular cylinder of length L and radius r , a_r can be chosen as the semiempirical relation [27]

$$a_r = 1.24 a_p \sqrt{\ln a_p}, \quad (2)$$

where a_p is the aspect ratio $a_p = L/2r$. The orbit parameter C ranges from 0 to ∞ , with $C = 0$ corresponding to $\theta = 0$, i.e.,

perfect alignment of the fiber with the z axis, and $\theta = \pi/2$ and $C = \infty$, corresponding to rotation in the xy plane. This range is transformed to $[0, 1]$ by introducing the orbit constant

$$C_b = \frac{C}{C + 1}. \quad (3)$$

The analytic solution [2] for an ellipsoid in a shear flow is

$$\phi = \tan^{-1} \left(a_p \tan \frac{a_p G t}{1 + a_p^2} + C_\phi \right), \quad (4)$$

$$\theta = \tan^{-1} \left(\frac{a_p C_\theta}{\sqrt{a_p^2 \cos^2 \phi + \sin^2 \phi}} \right), \quad (5)$$

where G is the shear rate and t is time. The constants C_ϕ and C_θ are determined from the initial position of the object, $C_\phi = \phi_0$ and $C_\theta = \tan(\theta_0)$.

Figure 2 shows the analytical and numerical solutions of the LBM of the motion of a rodlike object, with length l , aspect ratio $a_p = 3$, at four different resolutions. The spatial resolution of fluid flow is given by $\Delta = \delta_x/l = 1/2.4, 1/6, 1/9$, and $1/12$ (corresponding to case No. 1A, No. 2A, No. 3A, and No. 4A in Table I). Here δ_x is the step of spatial discretization. Note that the fiber length in lattice units (L) is related to the resolution as $\Delta = 1/L$. The discretization of the fibers is measured by $\Delta_s = 2\pi r/N_n \Delta$, where N_n is the number of nodes on a hinge and r is the radius of the fiber. We set $\Delta_s = 1.2\Delta$ in order to avoid the possibility that there are two Lagrangian nodes in a lattice cell. This implies that N_n increases if the resolution increases and Δ become smaller. The

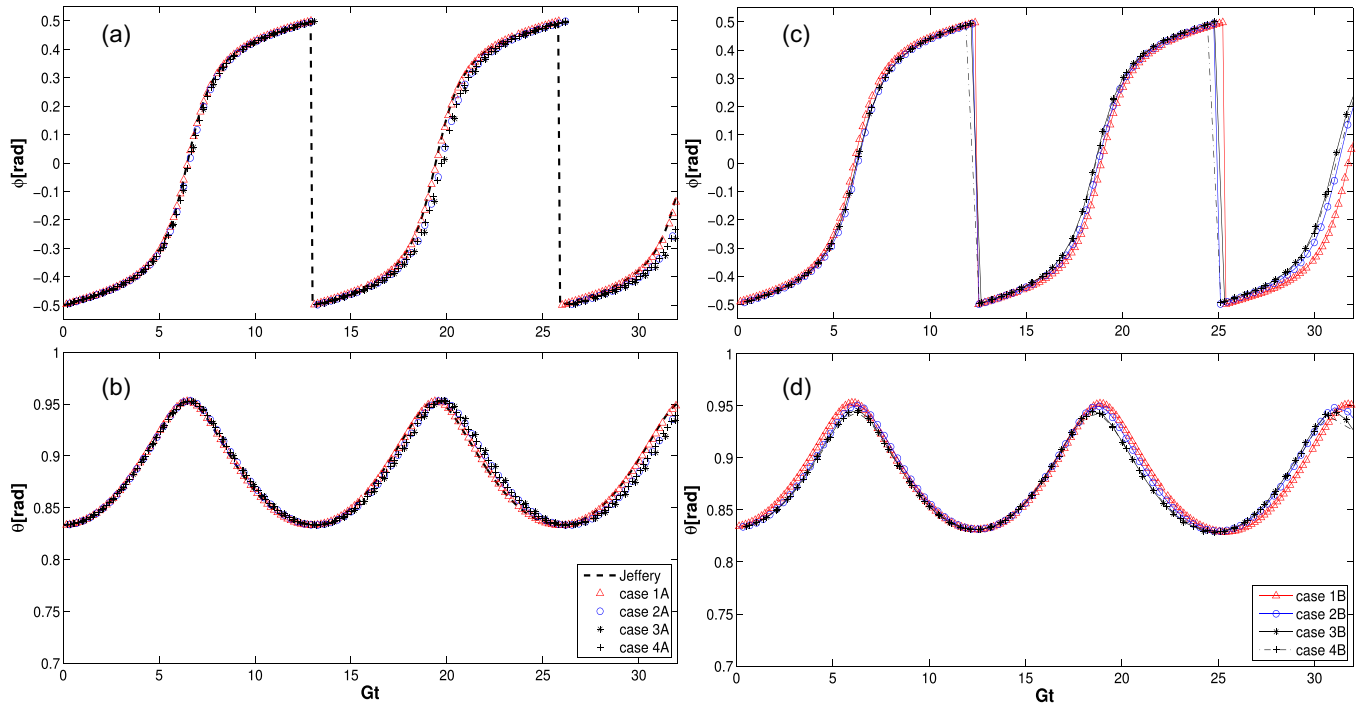


FIG. 2. (Color online) (a–b) Comparison of LBM-EBF simulation results (symbol) for the angle ϕ (a) and θ (b) with Jeffery's analytic solution for an ellipsoid given by Eq. (4) and Eq. (5) (dashed line). The particle Reynolds numbers and the aspect ratio of the fibers in LBM-EBF simulation are fixed, $Re_p = 0.005$ and $a_p = 3$. The aspect ratio used on Jeffery's analytic solution is $a_r = 3.89$. (c–d) Convergence test for the simulation of a rodlike fiber, aspect ratio $a_p = 3$, $Re_p = 5$, $\theta_0 = \pi/6$, and $\phi_0 = -\pi/2$.

TABLE I. Simulation parameters for the test cases. r is the radius of the rod (lattice unit), N_h is the number of hinges on a rod, N_n is the number of nodes on a hinge, Re_p is the fiber Reynolds number, T is orbit period, and T_{err}^J and T_{err}^4 are the differ orbit period with the Jeffery's period and with the period of case 4B, respectively.

	1A	2A	3A	4A	1B	2B	3B	4B
$2r$	0.8	2	3	4	0.8	2	3	4
Δ	1/2.4	1/6	1/9	1/12	1/2.4	1/6	1/9	1/12
N_n	3	5	7	9	3	5	7	9
N_h	3	5	7	9	3	5	7	9
Re_p	0.005	0.005	0.005	0.005	5	5	5	5
T	12.78	12.91	13.14	12.89	12.83	12.46	12.42	12.40
T_{err}^J	1.24%	0.24%	1.54%	0.39%				
T_{err}^4					3.4%	0.5%	0.15%	0%

initial position of the rod object is $\phi_0 = -\pi/2$ and $\theta_0 = \pi/6$ for all cases. The fluid flow is initialized as a simple shear flow with shear rate G at $t = 0$. The particle Reynolds number is kept constant at $\text{Re}_p = Gl^2/\nu = 0.005$ for all cases; i.e., the cases No. 1A–4A describe the same problem with increasing resolution of both fluid and solid spaces.

In Fig. 2, the computational results of a rodlike object with aspect ratio $a_p = 3$ and Jeffery's analytical solution with aspect ratio $a_r = 3.89$ obtained from Eq. (2) show a good agreement for both the rotation angles ϕ and θ . There is a maximum difference of 1.5% between the simulated orbit period and the analytical orbit period (T_{err}^J) for all four cases.

There are no analytical predictions for validation in case of finite Re_p . Therefore, we have performed an additional convergence test for four different spatial resolutions like before for a representative single fiber in a shear flow, i.e., cases No. 1B–4B in Table I. The particle Reynolds number and the aspect ratio are kept constant at $\text{Re}_p = 5$ and $a_p = 3$ representative for the turbulent flow that is of interest here. The initial position of the fiber is $\phi_0 = -\pi/2$ and $\theta_0 = \pi/6$. Figure 2(c)–(d) shows the numerical results for four different grid resolutions of the fiber. The results obtained with different grid resolutions agree well with each other. Especially, the solutions of cases No. 2B–3B are nearly the same as for the highest resolution case No. 4B. The orbit period error when compared with case No. 4, T_{err}^4 , is less than 0.5% for those cases and about 3.4% for the coarsest resolution, case No. 1B. Therefore, we believe that even with the coarsest resolution the fiber-flow interactions are sufficiently well resolved, in particular for the problem addressed hereafter, and set the fiber resolution in our next simulations to $0.8\delta_x$ for the diameter of the fiber.

To demonstrate that the resolution of the fiber flow is sufficient for the cases we are studying, we analyze the fluid flow around fibers by extracting velocity values at the eight corners of a box as shown in Fig. 3. The fluid flow used for this analysis is obtained from the turbulent channel flow simulation presented later in the paper, case No. 1 in Table II. The difference between the fiber velocity, U_s , and the averaged fluid velocity from those eight corners, U_f , is computed and projected onto a plane normal to the “axis vector” of the fiber (plane P). The PDF of the projected normal velocity

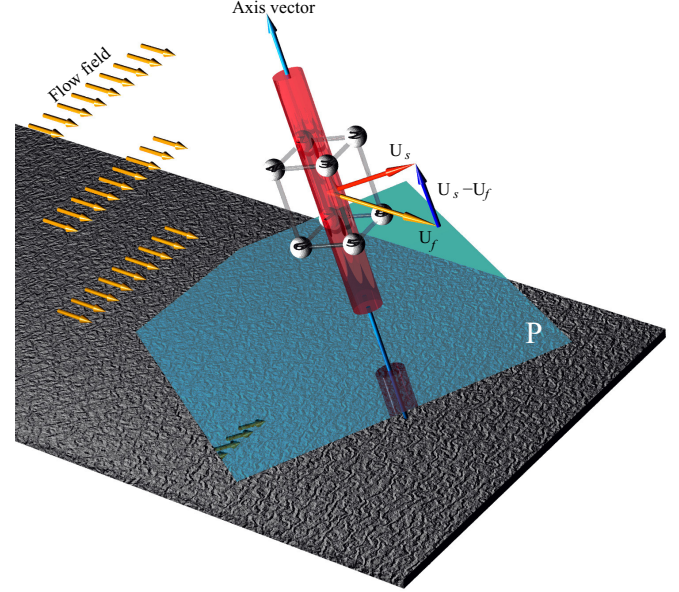


FIG. 3. (Color online) Sketch of the calculation for the fiber projected normal velocity.

$|U_s - U_f|_P$ is shown in Fig. 4(a). The shear rate over the fiber length and the fiber diameter is computed as $G = u_d/h$, where u_d is the difference in velocity between a pair of nodes in the sample box that cross through the fiber (see Fig. 3) in the cross-fiber or axis direction and h is the sample box size. The PDF of the particle Reynolds number, $\text{Re}_p = Gl^2/\nu$ is computed and shown in Fig. 4(b).

As shown in Fig. 4, the projected normal velocity around a fiber is small. $|U_s - U_f|_P^+ < 1$ for the fluid at a distance to the fiber of 1 to 2 fiber diameters. Since the diameter is $d^+ = 2$, the corresponding Reynolds number is obtained by multiplying the values in Fig. 4 by 2. This means that the flow around the fiber lacks a complex wake, and for all cases looked at here the particle Reynolds number based on the cross-fiber velocity is of order unity. Meanwhile, the flow around the fiber has a projected normal velocity less than one for the fluid at a distance to the fiber of a fiber length. The maximum in the PDF of the particle Reynolds number appears at $\text{Re} = 3$, for which it has been shown in the validation test case above that the selected fiber grid resolution is sufficient.

B. Single-phase flow simulation

In this section a DNS with the lattice Boltzmann model of a single-phase, fully developed, plane turbulent channel

TABLE II. Fiber parameters for the LBM simulations.

Case	N_p	a_p	L^+	v_f [%]	$\alpha = n_p L^3$	r_p	St	St ⁺
No. 1	4752	15	24	0.11	0.325	1.2	0.245	2.33
No. 2	11 800	6	9.6	0.11	0.052	1.2	0.181	1.72
No. 3	35 640	2	3.2	0.11	0.006	1.2	0.110	1.04
No. 4	44 642	6	9.6	0.43	0.195	1.2	0.181	1.72
No. 5	35 640	2	3.2	0.11	0.006	1.0	0.091	0.87

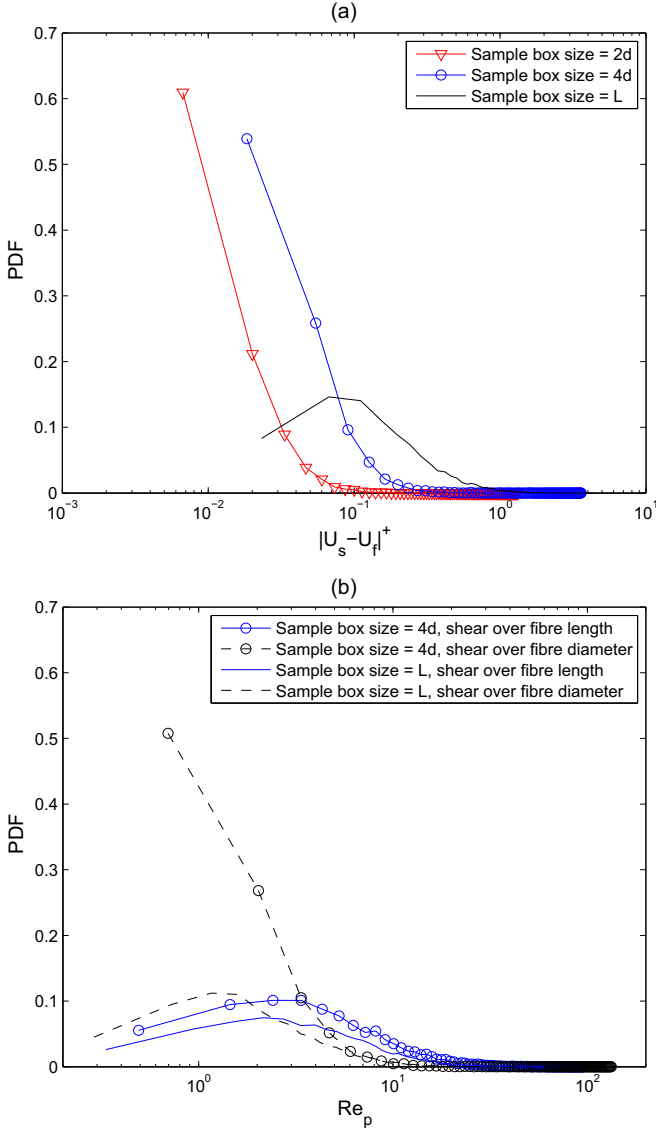


FIG. 4. (Color online) The PDF of the projected normal velocity (a) and particle Reynolds number (b) of fibers in the turbulent channel flow.

flow is compared to a DNS performed with a conventional spectral method. The friction Reynolds number of the flow, which is based on the friction velocity u_τ and the channel half-width δ , in both simulations is $Re_\tau = 180$. The spectral DNS code uses Fourier expansions with periodic boundary conditions in both streamwise and spanwise directions and Chebyshev polynomials in the wall-normal direction and has been extensively validated [28].

The computational domain of the LBM simulation and spectral DNS is the same and is $8\delta \times 2.2\delta \times 2\delta$ in the streamwise, spanwise, and wall-normal directions, respectively. This is sufficient to sustain a turbulent flow and obtain accurate turbulent statistics [29]. The grid size in wall units in the spectral DNS varies from 0.1 at the wall to 5.84 at the center line of the channel, and $\Delta x^+ = 12$ and $\Delta z^+ = 6.2$, where $^+$ denotes normalization by ν/u_τ . The grid resolution in the LBM simulation is kept constant at $\Delta^+ = 2$ in each

direction. This leads to $120 \times 97 \times 64$ collocation points in the spectral DNS and $710 \times 180 \times 198$ grid points in the LBM simulation, respectively, giving a total of about 26 million lattice cells. A constant body force is applied in the streamwise direction to drive the fluid flow with a small Mach number $Ma = |\mathbf{u}|/c_s = 0.03$, to ensure incompressible flow conditions in the LBM. Periodic boundary conditions are used in the streamwise and spanwise directions, and a no-slip boundary condition is applied on the channel walls. The turbulent statistics were collected during a total of 35 characteristic times ($t^* = \delta/u_\tau$), after the simulation reached a statistically stationary state. The averaging is performed both spatially and temporally.

Figure 5(a) shows a comparison of the mean velocity profile of LBM simulations (with two different grid resolutions, $\Delta^+ = 2$ and $\Delta^+ = 1.5$) with spectral DNS results. Both LBM simulations show a good agreement with the DNS results. Only 1% difference is found between LBM and DNS results for the mean velocity profile. The root-mean-square of the streamwise, wall-normal, and spanwise velocity fluctuations (normalized by u_τ) u_{rms}^+ , v_{rms}^+ , and w_{rms}^+ are plotted in Fig. 5(b). The agreement between the two LBM results and the spectral DNS is again very good. Figure 5(c) and 5(d) shows profiles of the Reynolds shear stress and pressure fluctuations, respectively. In general, the results from the LBM simulation match the spectral DNS results very well, and only small differences (less than 0.7%) are found in the buffer region, $y^+ < 40$, for the Reynolds stresses while the differences in pressure fluctuations are within 0.2% to 1% near the wall and within 2.5% near the location of the peak pressure variance around $y^+ = 35$. These comparisons show that the LBM simulation correctly describes fully turbulent channel flow in terms of first and higher order single-point statistics.

III. TWO-PHASE FLOW SIMULATION: RESULTS AND DISCUSSION

This section presents numerical results of LBM simulations of turbulent channel flow with rigid, finite size fibers or rods at $Re_\tau = 180$. The fibers are introduced into the fully developed turbulent single-phase flow at time t_0 with an initial translational velocity and angular velocity equal to the fluid velocities found at the location of each fiber. Statistics were collected after the flow and suspension had reached a statically steady state. All cases were run in the same computational domain ($8\delta \times 2.2\delta \times 2\delta$ in the streamwise, spanwise, and wall-normal directions, respectively) and same resolution $\Delta^+ = 2$. The number of fibers and the summary of input parameters are given in Table II. Here N_p , a_p , L , and v_f are the number of fibers, their aspect ratio, fiber length, and volume fraction, respectively. The concentration parameter α is related to the fiber number density n_p and fiber length L by $\alpha = n_p L^3$. Different fiber lengths ($L^+ = 24, 9.6$ and 3.2 , cases No. 1, No. 2, and No. 3 in Table II) have been used for comparison. The volume fraction of fibers is $v_f = 0.11\%$ up to 0.44% , and density ratio between fiber (ρ_f) and fluid (ρ_l) is $r_\rho = 1.0$ or 1.2 . The density ratio $r_\rho = 1.2$ is chosen to mimic cellulose fibers in water. In our model the gravity is not included. Therefore, the density ratio influences only inertial dynamics and not fiber settling. The driving force (pressure gradient) used in

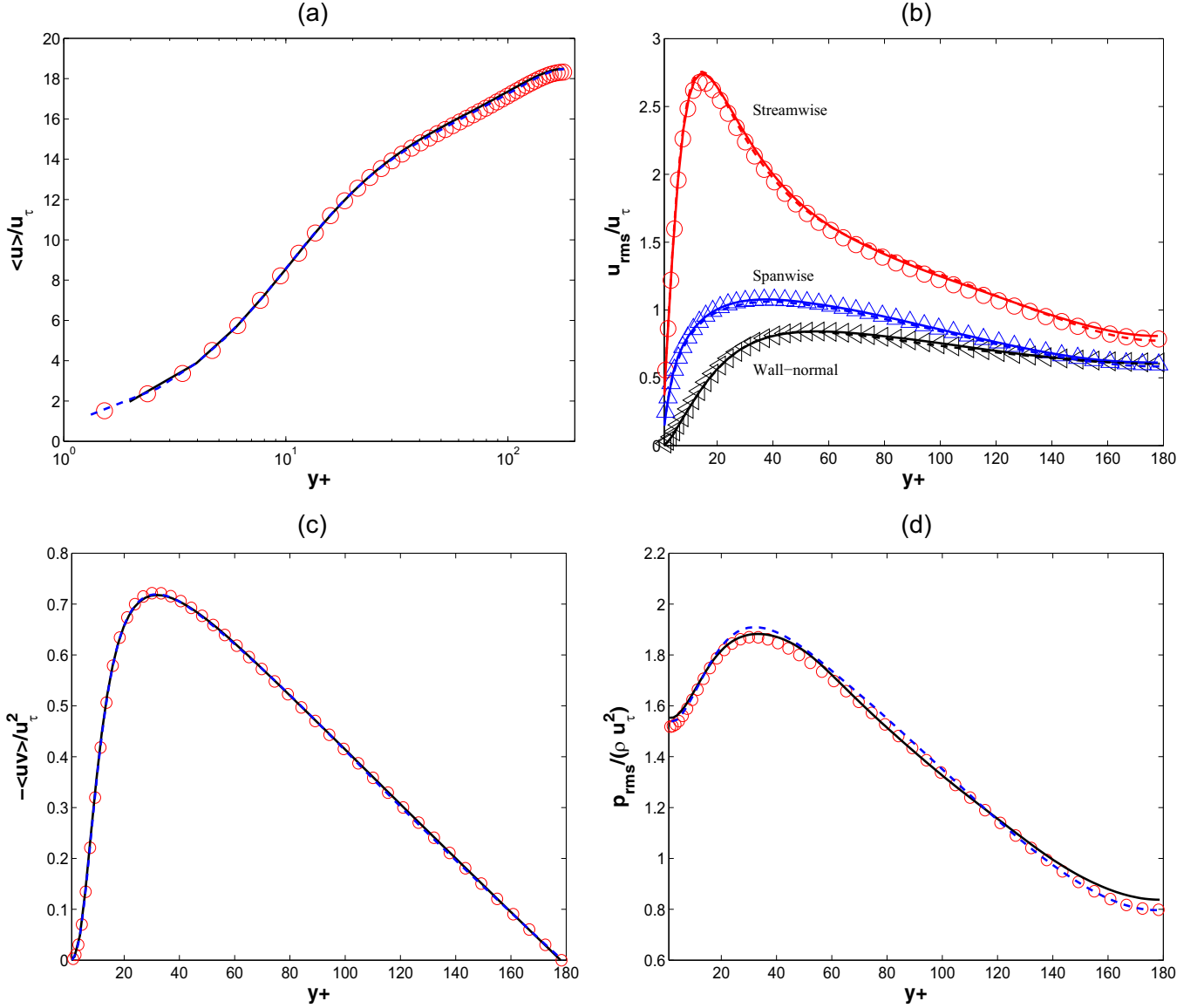


FIG. 5. (Color online) Turbulent statistics of channel flow at $Re_\tau = 180$. Symbols present the spectral DNS results, the solid line is the LBM result with $\Delta^+ = 2$, and the dashed line is the LBM result with $\Delta^+ = 1.5$. (a) Mean velocity profiles; (b) streamwise, spanwise, and wall-normal velocity fluctuations; (c) Reynolds shear stress; (d) root-mean-square of pressure fluctuations.

these cases is kept the same as the driving force used in the single-phase flow case. The fibers were modeled by six nodes on a hinge, and the number of hinges was selected to ensure that the distance between two hinges is not larger than a lattice unit.

For a rigid cylindrical fiber, the volume is $V_p = \pi R^2 L$. Therefore, the volume fraction can be derived from

$$v_f = \frac{V_p N_p}{V_\Sigma} = n_p V_p = \pi \frac{n_p L^3}{4a_p^2}, \quad (6)$$

where V_Σ is the total volume of fluid and $n_p = N_p / V_\Sigma$ is the fiber number density.

We define a fiber Stokes number based on the fiber response time, τ_p [14], and the bulk flow time scale $\tau_f = 1/\dot{\gamma}$, where $\dot{\gamma}$ is a shear rate of the bulk flow ($\dot{\gamma} = |\mathbf{u}|/\delta$). We also formulate a near-wall Stokes number using the near-wall time

scale $\tau^+ = \nu/u_\tau^2$:

$$\tau_p = \frac{2\rho_f L^2 \ln(a_p + \sqrt{a_p^2 - 1})}{9\rho_l \nu a_p \sqrt{a_p^2 - 1}}, \quad (7)$$

$$St = \frac{\tau_p}{\tau_f}, \quad St^+ = \frac{\tau_p}{\tau^+}. \quad (8)$$

Table II lists the fiber parameter values for the simulations performed. Note that the bulk Stokes number St is of the order of 0.1, while the near-wall Stokes number is always less than 3.

In order to analyze the motion of the fibers, we have recorded the fiber statistics at every five time steps. Statistical quantities such as mean velocity, fluctuation intensities, Reynolds shear stress, etc., were then computed based on one

million samples, equivalent to the recording time $t = 30t^*$, to make sure that the fiber distribution achieved a statistically steady state. To analyze the carrier phase, the fluid quantities were stored every 10 time steps. Here the averaging was performed over the entire composite flow field, i.e., containing the regions of fluid and immersed fibers together, since the statistical difference between the composite fluid and the fluid is very small [17,18].

A. Turbulent flow of a fiber suspension

The streamwise mean velocity profiles of fibers $\langle u_f \rangle$ and fluid $\langle u_l \rangle$ for cases No. 1, No. 2, No. 3, and No. 5, referring to the cases listed in Table II, are shown in Fig. 6 as function of wall-normal position. The velocities of the fibers are computed at the center of mass. The volume fraction is constant at 0.11% in all cases, while the concentration parameter α varies; see Table II. The α values seen in Table II indicate that fiber-fiber interactions have a small influence in these cases [7].

Away from the wall, in the outer region, the differences in mean fluid and particle velocity are very small. The fluid mean velocity profiles collapse onto a single curve in the near-wall region, as one should expect, since the volume fraction of fibers is small in all cases. In the near-wall region the fiber mean velocity shows an excess over the fluid velocity, that increases with increasing fiber length. We show later that up to a distance $2L^+$ from the wall, the excess velocity is caused by a preferential accumulation of the fibers in high-speed near-wall turbulent streaks. This result contrasts with earlier results by Mortensen *et al.* [9], where inertial effects dominated. In their simulation, the mean velocity of point-like, fast response prolate ellipsoidal particles ($St^+ = 5$) is lower than the corresponding mean fluid velocity in the near-wall region due to a preferential accumulation in low-speed streaks. Particles with larger inertia, e.g., $St^+ = 30$, have a mean velocity greater than the corresponding mean fluid velocity only in the viscous sublayer in their simulation, while further

away from the wall the particles are slower than the fluid. In our case, however, the inertial effect is small since the fibers are almost neutrally buoyant (cases No. 1–3) or completely neutrally buoyant (case No. 5) and the corresponding Stokes numbers are small ($St^+ < 3$). Consequently, the streamwise mean fiber velocity of case No. 3 and case No. 5 are almost the same. The long fibers have the highest velocity in the near-wall region outside the viscous sublayer. Close to the wall the long fibers lose momentum due to interactions with the walls, and therefore they are slower than the short fibers. At the innermost points the probability of observing a fiber is very low; i.e., no fibers with $L^+ = 24$ could be found below $y^+ \approx 4$ during the whole simulation time, due to interactions with the wall.

Figure 7 exhibits profiles of the turbulence intensities of the fluid (a) and fiber phase (b) for cases No. 1, No. 2, and No. 3 in Table II. As seen from Fig. 7(a), the peak in the streamwise fluid velocity fluctuations (u_{rms}) around $y^+ \approx 15$ is attenuated by the effect of the fibers, whereas the spanwise and wall-normal components are hardly affected. The number of fibers in case No. 1 is much smaller than in case No. 3 but the reduction of streamwise fluid fluctuations is similar, suggesting that fibers can effectively damp turbulence if their length becomes comparable to the size of the near wall turbulence structures. In Fig. 7(b), it is seen that the intensity of streamwise fluctuations of the fibers is substantially lower than that of the fluid in the buffer layer, especially for the longest fibers. Fiber fluctuations are thus reduced if the fiber length becomes similar to the turbulent length scales even when the Stokes number is small and fiber dynamics is not dominated by inertia. Only very close to the wall, up to $y = 1/2L$, fiber fluctuations are larger than the fluid fluctuations due to interactions with the wall. These results are different to earlier findings for pointlike particles [9], where it was found that heavy fibers have a higher fluctuation intensity than light fibers, but in their simulations particle inertia was the dominant factor. The effects of the fibers on the Reynolds stresses are nevertheless moderate in the present simulations, but stronger effects are observed in ongoing simulations at higher values of α .

Figure 8 illustrates turbulent vortices in the flow field by means of isosurfaces of the second invariant, Q , of the velocity gradient tensor ($\nabla \mathbf{u}$),

$$Q = \frac{1}{2}(\|\boldsymbol{\Omega}\|^2 - \|\mathbf{S}\|^2), \quad (9)$$

where $\|\mathbf{S}\| = [\text{tr}(\mathbf{S}\mathbf{S}^T)]^{1/2}$, $\|\boldsymbol{\Omega}\| = [\text{tr}(\boldsymbol{\Omega}\boldsymbol{\Omega}^T)]^{1/2}$, and \mathbf{S} and $\boldsymbol{\Omega}$ are the symmetric and antisymmetric parts of $\nabla \mathbf{u}$. In the suspension flow [Fig. 8(b)] the large-scale vortices appear similar to those in the single phase flow [Fig. 8(a)], but the fibers generate a lot of small-scale vorticity. This vorticity is due to the fiber-flow and the fiber-wall interaction, which generates an angular motion of the fiber and influences the fluid around it.

One-dimensional streamwise energy spectra of the streamwise velocity at $y^+ = 19$ are shown in Fig. 9. In the case with fibers the energy at high wave numbers is higher than in the case without fibers, which confirms the observation in Fig. 8 that fibers induce small-scale fluid motions. Note that the energy spectrum for the case without fibers shows very

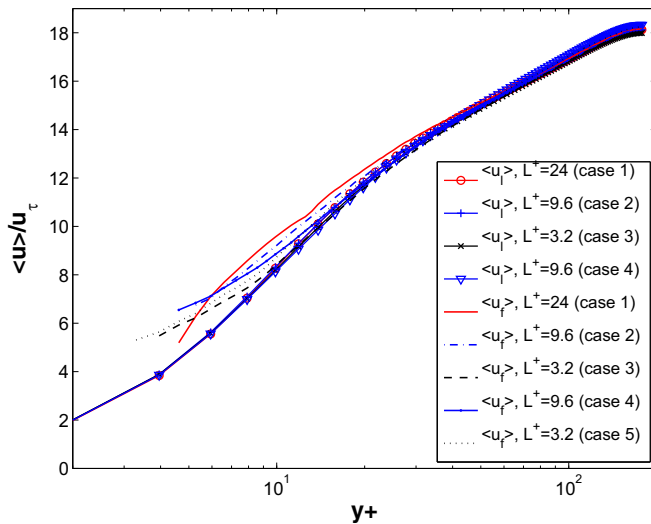


FIG. 6. (Color online) Streamwise mean velocity profiles of fiber $\langle u_f \rangle$ and fluid $\langle u_l \rangle$ for the cases listed in table II, No. 1, No. 2, No. 3 ($r_\rho = 1.2$), and No. 5 ($r_\rho = 1.0$).

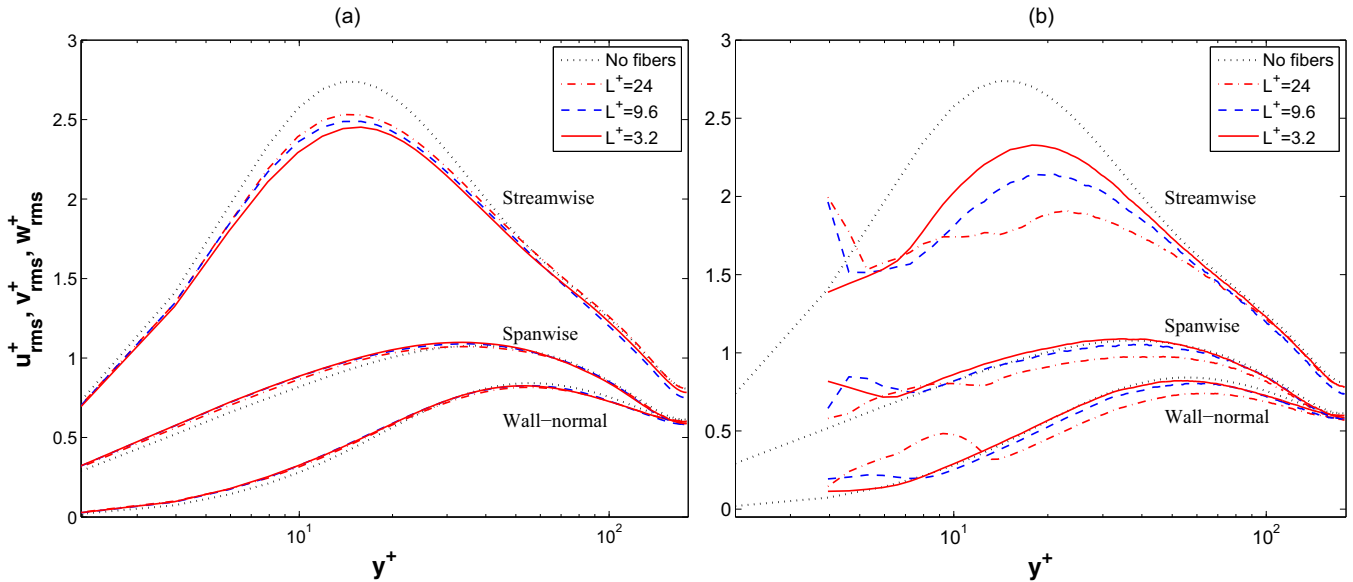


FIG. 7. (Color online) Root-mean-square values of the streamwise, wall-normal, and spanwise fluctuating fluid velocity components (a) and fiber velocity components (b) normalized by u_τ for different fiber lengths.

good agreement with the one [30] plotted in Fig. 9, giving further evidence that the turbulence is well resolved.

Figure 10 shows a three-dimensional view of the instantaneous fluid velocity and fiber distribution for fibers with a

distance to the wall less than $1.5L$ for case No. 4. The color field at the bottom of Fig. 10 is the magnitude of flow velocity at the slice $y^+ = 14.4$, and reveals the high- and low-speed streaks as red and blue bands extending in the streamwise direction, which also correspond to the ridges in the isovelocity surfaces. We can observe that fibers are predominantly found in high-speed streaks, implying that when finite-size fibers move towards the wall by sweeplike motions into high-speed streaks, they tend to stay there.

In order to quantify the accumulation of the fibers in high-speed streaks we divide the near-wall region $y^+ \leq 16$ into six slabs and compute the streamwise velocity of the fiber at its center of mass identified in one of these slabs. We then

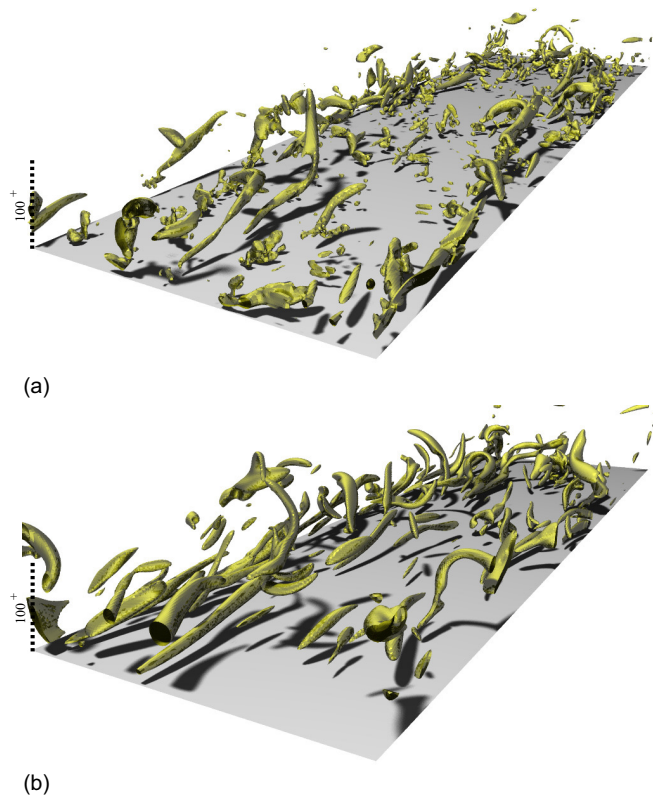


FIG. 8. (Color online) The isosurface of the second invariant $Q = 0.45$ of $\nabla \mathbf{u}$ for (a) the case without fibers and (b) case No. 1. The dimensions of the wall surface (gray color) are 1420 and 396 wall units in x and z directions.

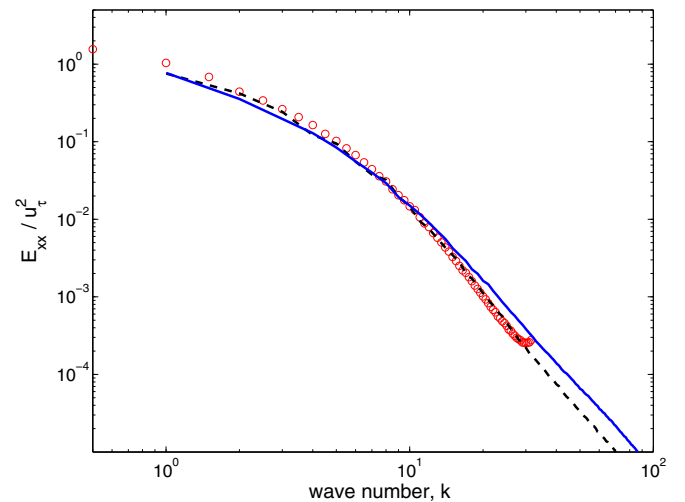


FIG. 9. (Color online) Comparison between the streamwise one-dimensional spectra of the streamwise velocity fluctuation of single-phase flow (dashed line) and suspension flow (solid line, case No. 1) at location $y^+ = 19$; \circ DNS data [30] for $Re_\tau = 180$. The wave number is here scaled by the streamwise box size.

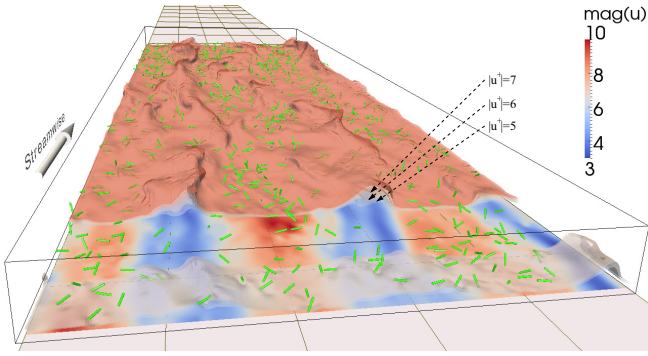


FIG. 10. (Color online) Three-dimensional view of case No. 4, fiber length $L^+ = 9.6$, $v_f = 0.43\%$. The fibers shown here are fibers with a distance to the wall less than $1.5L$. The dimensions of the outlined box are 1420, 64, and 396 wall units in the x , y , and z direction, respectively, and the three closely spaced isosurfaces mark surfaces where the fluid velocity $|\mathbf{u}^+| = 5, 6, 7$.

subtract the mean streamwise fluid velocity in that slab to obtain the velocity fluctuation of the fiber u'_f with respect to the mean flow velocity. Since the fiber velocity and local fluid velocity at the fiber position are nearly the same we can regard u'_f as the fluid velocity fluctuation at the position of the fiber. The probability density function (PDF) of u'_f of all fibers in the specified near-wall region for cases No. 1–3 are shown in Fig. 11(a). All PDFs and most strongly the ones of the longer fibers are biased towards positive u'_f implying that fibers indeed tend to accumulate in regions with a higher than average fluid velocity, i.e., high-speed streaks, as indicated by Fig. 10. This accumulation of fibers in high-speed streaks explains why fibers move faster than the mean fluid velocity near the wall.

The obvious question is, why are almost neutrally buoyant fibers accumulating in high-speed streaks? Visualizations suggest that when the finite-size fibers move towards the wall by a turbulent sweep into a high-speed streak a part of them collide with the wall and are pushed back or at least prohibited from following the fluid sideways into a low-speed streak. To find evidence for this process we also show in Fig. 11(a) the PDF of the streamwise velocity fluctuation u'_f (solid line) of the fibers for case No. 1 ($L^+ = 24$) but now only for the fibers that have contact with the wall. Since the PDF is biased towards positive u'_f we can conclude that especially fibers in high-speed streaks touch the wall, in support of the previous observation. Figure 11(b) shows the PDFs of the angular fiber velocity Ω_z about the spanwise axis for both fibers having contact and not having contact with the wall in the region $y^+ \leq 16$. The mean wall distance of the center of mass for the two fiber classes is similar. The figure reveals that these wall collisions have a significant effect on fiber motions; fibers with wall contact have generally a much higher Ω_z and have a similar angular velocity as the mean flow near the wall when they touch the wall and flip over. As mentioned before, this interaction with the wall is inelastic if the fiber moves mostly parallel to the wall, but the collisions are approximately elastic when the fibers have a high velocity towards the wall leading to significant repulsive forces and changes in angular fiber velocity. We can anticipate

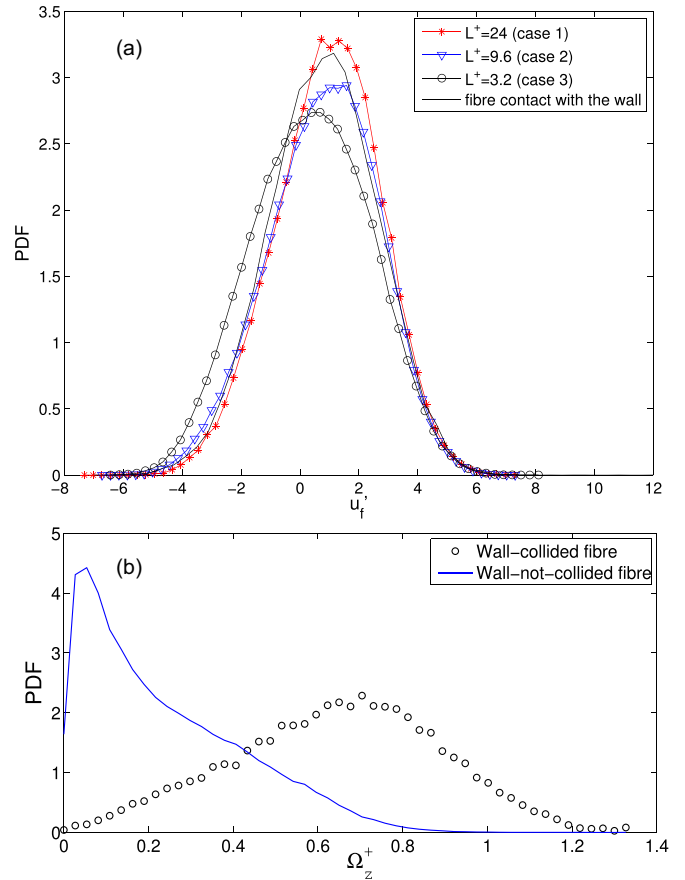


FIG. 11. (Color online) (a) PDFs of u'_f of all fibers in the region $y^+ \leq 16$ for cases No. 1–3 (lines with symbols) and PDF of u'_f of fibers that have contact with the wall in case No. 1 (solid line). (b) PDFs of Ω_z for fibers with (symbols) and without (solid line) contact with the wall in case No. 1. Only fibers in the region $y^+ \leq 16$ are considered and Ω_z has been scaled with v/u_τ^2 .

that in cases with more inelastic collisions with the wall and weaker repulsive forces the accumulation of the fibers in the high-speed streaks is less strong and hence the difference between fluid and fiber mean velocity is smaller. This could be a topic of future research. All these results support the idea that when finite-size fibers move towards the wall in turbulent sweeps contact forces with the wall hinder the fibers from passively following the fluid towards low-speed flow regions and tend to keep them in high-speed flow regions. Other effects like fiber-fiber interactions and the feedback of the fibers on the flow play likely a minor role in causing the difference between the mean fluid and fiber velocity near the wall since the concentration parameter α is small in the simulations. This is confirmed by comparing case No. 2 and No. 4 with the same fiber size. The same fiber mean velocity is observed near the wall (Fig. 6) although α and the fiber volume fraction and thus the fiber-fiber interactions and fiber feedback are different in these two cases.

It should be noted that these results are different from earlier ones [9,10], where the authors studied very small fibers treated as one-way coupled point particles, in a parameter range where fiber inertia was important. Under those conditions it was found that fibers accumulate in low-speed instead of

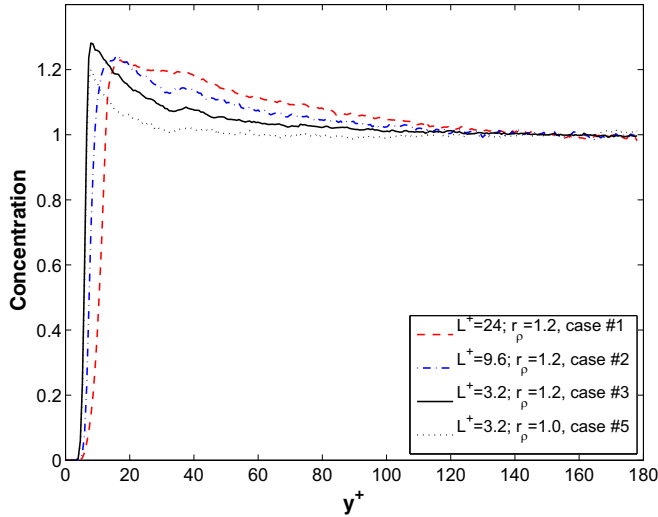


FIG. 12. (Color online) The fiber concentration profile across the half channel for different fiber lengths.

high-speed streaks. Marchioli *et al.* concluded that for the cases they studied, the segregation was mainly caused by the fiber inertia while the fiber aspect ratio had little influence. We note that the segregation of fibers is fundamentally different in our and their study, and that the present results shed new light on the effects of a finite fiber length.

B. Near-wall fiber accumulation

In order to analyze the distribution of the fibers across the channel, we divided the channel into 540 slices in the wall normal direction. The fiber concentration is computed from the total number of fibers present in each slice during a time $t = 30t^*$. Figure 12 shows the fiber concentration profile across the channel normalized with the mean concentration at the channel center. In all cases we observe that the fibers accumulate near the wall at a distance of the order of the fiber length from the wall. The neutrally buoyant case and the case with $r_p = 1.2$ have a maximum accumulation at the same distance, $2.2L$, from the wall, but the heavier fiber shows a stronger accumulation indicating that there is some turbophoresis effect. However, finite size effects also play a role since we observe accumulation for $r_p = 1.0$ as well. Results presented below indicate that finite size fibers moving towards the wall region spend a relatively long time there due to the difficulties of escaping the near wall high-speed regions. The excess concentration for the cases studied here is moderate, of the order of 25%, which is much smaller than, e.g., the turbophoresis effect for heavy particles in gas flow [10].

Collisions with the wall seem to explain the accumulation in high-speed streaks. To study this effect, details of the movement of one individual fiber of length $L^+ = 24$ near the wall are plotted in Fig. 13. During most of the time the fiber moves at roughly constant speed and angular velocity, but it sometimes abruptly changes its direction of motion and rotation. Four of these instants are marked as vertical dashed lines.

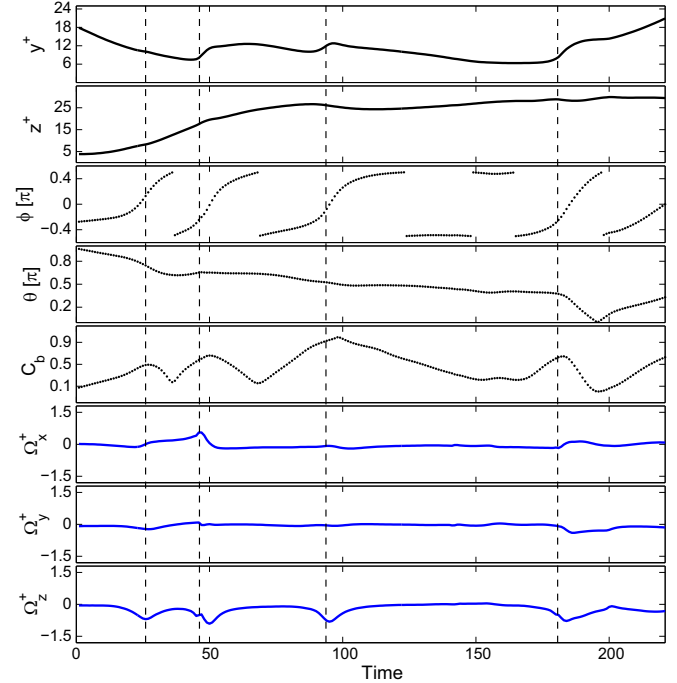


FIG. 13. (Color online) Time history of a fiber moving in the vicinity of the wall. Fiber length $L^+ = 24$. The top two panels show the position y^+ and z^+ of the fiber center in the y - z plane, and the three below show the orientation of the fiber (ϕ and θ angles and orbit constant C_b). The bottom three show the angular velocity Ω around each of the three axes.

At the first instant (at time ≈ 25), the fiber does not touch the wall, but we still observe a large change of the rotation speed Ω_z about the z -axis because the fiber enters a strongly vortical flow region (note the rotation angles ϕ and θ in this figure), whereas the trajectory of the fiber remains almost unchanged. Between $t = 40$ and 200 the fiber follows a kayaking motion since the angle θ is around 50 degrees. At the second instant at $t \approx 50$, the center of the fiber is at $y^+ = 7$ and one side of the fiber has made contact with the wall. The high shear rate in the viscous sublayer and the collision force acting on one side of the fiber generates a large torque and changes the angular speed and pushes the fiber upward. However, the upward motion ends soon because the fiber is still in a high-speed streak where the fluid is moving toward the wall. This process is repeated several times, at $t \approx 90$ and $t \approx 180$, until the fiber escapes into an ejection-like outflow region and moves far away from the wall. The probability of seeing fibers in the near-wall region is thus higher than in the core region because the fibers apparently cannot easily escape the near wall region via turbulent ejections when they are trapped in the high-speed regions due to wall interactions.

C. Fiber orientation

The PDF of the orbit constant, C_b , at different wall-normal positions and for different fiber lengths is plotted in Fig. 14. PDF profiles were computed by subdividing the channel in 100 equal slabs in the wall-normal direction and calculating the histogram of C_b of all fibers in each slab during a time period

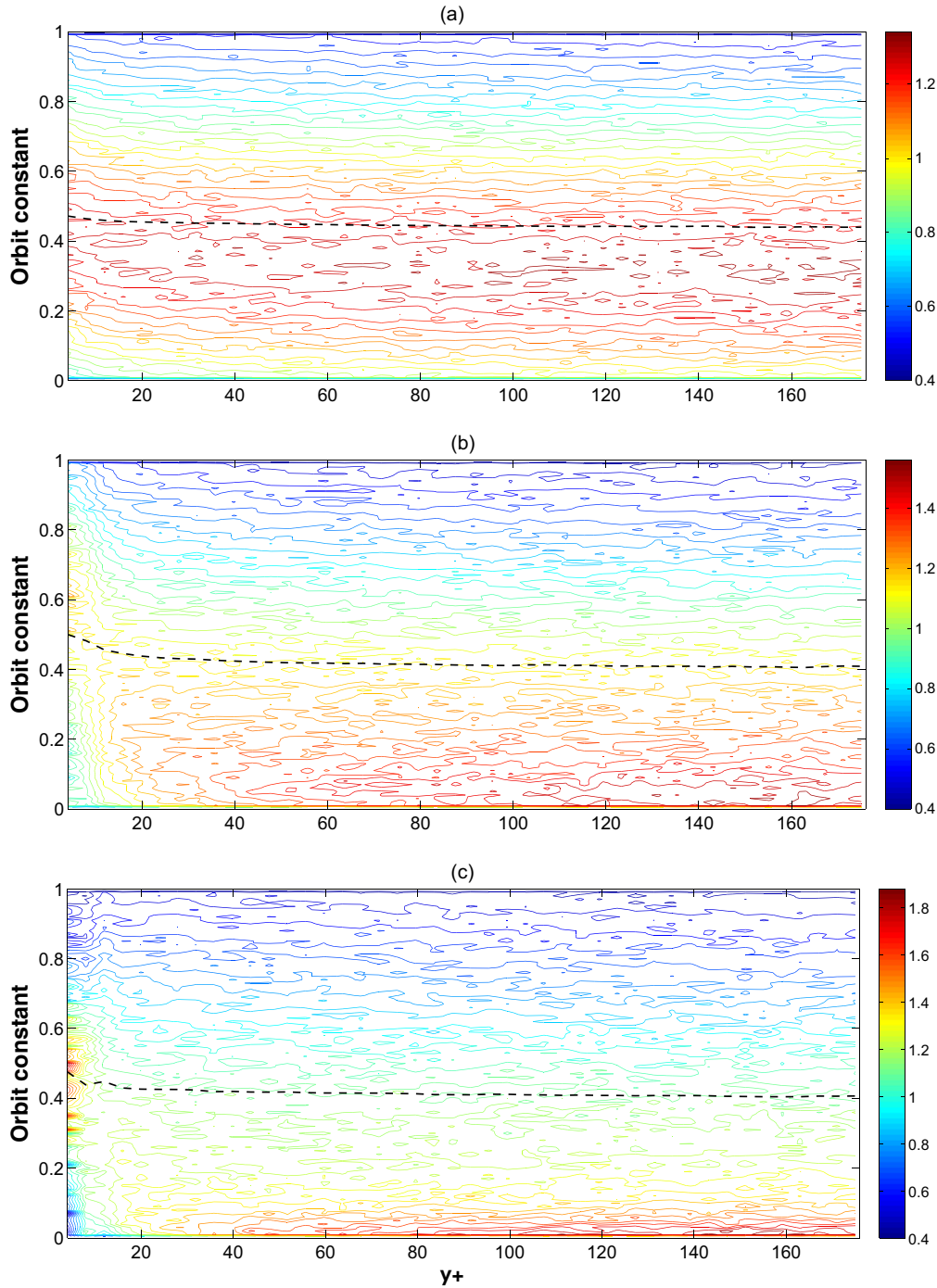


FIG. 14. (Color online) Probability density function of the orbit constant (contour lines) for fiber length $L^+ = 3.2$, case No. 3 (a); $L^+ = 9.6$, case No. 2 (b), and $L^+ = 24$, case No. 1 (c). The dashed line is the average orbit constant.

$t = 30t^*$. The calculated histogram is normalized by the total number of fibers located in each slab, and the dashed line in the figure is the average orbit constant, $\langle C_b \rangle$. At the center of the channel $\langle C_b \rangle = 0.45, 0.42$ and 0.40 for fiber length $L^+ = 3, 2, L^+ = 9.6$, and $L^+ = 24$, respectively, which is quite close to $\langle C_b \rangle = 0.5$, corresponding to a fully random orientation. The PDFs of C_b have a wide distribution, signifying that all orientations are possible.

For short fibers ($L^+ = 3.2$) we see in Fig. 14(a) that the PDF is almost independent of the distance from the wall. High

shear near the wall has an effect, but the orientation does not deviate much from a fully random isotropic distribution in the rest of the channel. This is further illustrated in Fig. 15, showing the absolute value of the mean direction cosines, where γ_x, γ_y , and γ_z are the angles between fiber and axes of the coordinate system xyz . The trend in the profiles generally agrees with those shown by others [9,10,31]. When the fiber length increases in comparison to the turbulence scales we note a tendency in the outer flow region that the PDF becomes more skewed with a high probability for low values of C_b .

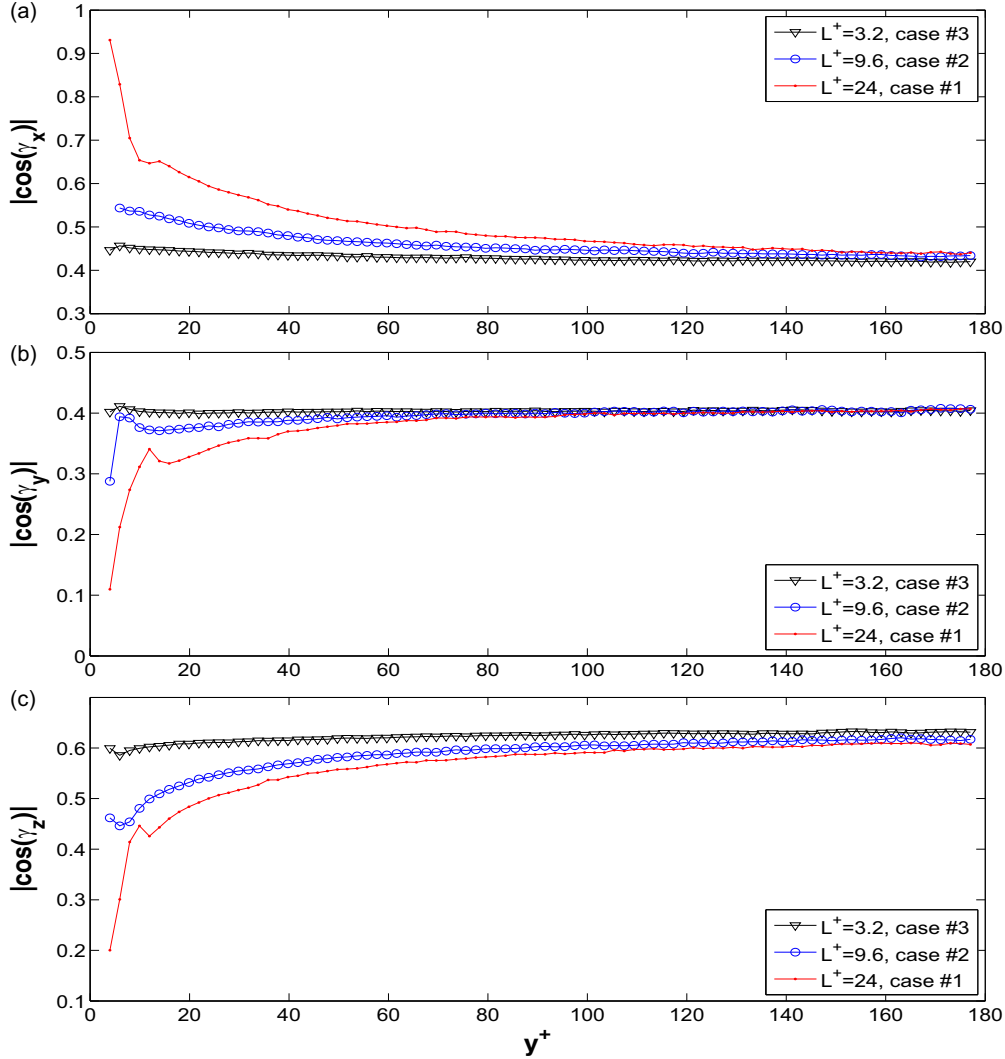


FIG. 15. (Color online) Mean values of direction cosines for three different fiber lengths, cases No. 3, No. 2, and No. 1 in Table II.

The maximum probability is found at $C_b \approx 0.3, 0.1$ and 0.05 for $L^+ = 3.2, 9.6$, and 24 , respectively. Hence, away from the walls we observe an increasing preference with increasing L^+ for a log-rolling type of motion. This alignment occurs despite the turbulent environment. However, the fiber orientation in our simulation agrees well with recent results of Rosén *et al.* [32] who showed that short and long fibers tend to have a tumbling and log-rolling motion, respectively. The transition between these two regimes is determined by a competition between fiber and flow inertia.

For the long fibers studied here we also see in Fig. 15(a) a clear trend of increasing values of $|\cos(\gamma_x)|$ in the near wall region, which implies a change from a log-rolling or kayaking type of motion to rotation in the shear plane as a wagging or flow-aligning motion. This is a natural consequence of the increased shear near the wall and high streamwise fluid velocity fluctuations, and agrees well with previous work [9,10,31]. When the distance of the fiber to the wall is less than half of its length, it cannot rotate freely in the shear plane and $\cos(\gamma_y)$ decreases to zero, which is characteristic of a fiber oriented along and rotating around the streamwise axis in a flow-aligning motion. Hence, finite size fibers tend to be

restrained to the x - z -plane [see Fig. 15(b)] and with increasing length to predominantly become aligned in the x direction [see Fig. 15(a), 15(c)].

IV. CONCLUSION

In this paper, we have conducted a DNS study of suspensions of rigid fibers in turbulent channel flow with the lattice Boltzmann model (LBM). The fibers or rods are of finite-size with a length from 3.2 to 24 in terms of viscous wall units. The fiber's interface is fully resolved with contact and lubrication force models for fiber-fluid, fiber-fiber, and fiber-wall interactions. Turbulence is accurately represented by the LBM simulation, as shown by good agreement with spectral DNS results for single-phase turbulent channel flow.

We found that the finite size of the fiber has a clear influence on the dynamics of the suspension. The statistical dynamics of the simulations show that the fibers accumulate in high-speed streaks near the wall, resulting in a mean fiber velocity that is higher than the mean fluid velocity. This preferential concentration is mainly caused by the interaction of the fibers with the wall and not by the inertial effects because the fibers

are almost or exactly neutrally buoyant and the Stokes number is small. The fluctuation intensities and orientation of the fiber are strongly influenced by the finite size, but the turbulence intensities of the fluid are only moderately influenced because of the low volume fraction and the small fiber Stokes number used in this simulation.

In the central region of the channel there is a strong tendency for fibers to have a kayaking type of motion, while close the wall they tend to rotate in the shear plane. Very close to the wall they become restrained to the wall-parallel plane and become predominantly aligned in the streamwise direction. This latter effect can be ascribed to the dominance of streamwise fluid velocity fluctuations and high shear rate in that region.

ACKNOWLEDGMENTS

We are grateful to Prof. Cyrus Aidun for discussions and for introducing us to the LBM-EBF model. Nicholas Apazidis and Fredrik Lundell are gratefully acknowledged for discussions and suggestions. We acknowledge support from EU COST Action FP1005. Computer time was provided by the Swedish National Infrastructure for Computing SNIC. Support by the Swedish Research Council VR (2011-5355, 2010-3938, 2010-4147, and 2010-6965) and PDC-KTH is gratefully acknowledged.

APPENDIX A: EXTERNAL BOUNDARY FORCED METHOD

In this appendix, we explain the EBF method in more detail. Let Ω_s and Ω_f represent the continuum domain for a fiber and the surrounding fluid. In Fig. 16 Ω_s and Ω_f are indicated by a set of circle and square symbols. Γ represents the fluid-solid boundary, and Γ_s and Γ_f are subsets for the solid and fluid boundary nodes (set of solid circles and solid squares,

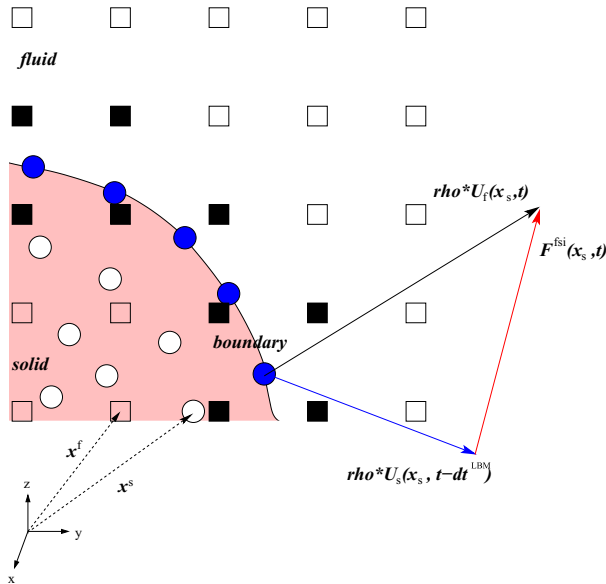


FIG. 16. (Color online) A schematic to illustrate the forces in EBF methods. Different symbols are employed to indicate the node types: circles: solid nodes; squares: fluid nodes; solid symbols: boundary nodes; and open symbols: interior nodes.

respectively in Fig. 16). To impose the no-slip boundary condition at the fiber surface we use the forces $\mathbf{F}_{f_{si}}(\mathbf{x}, t)$ and $\mathbf{g}(\mathbf{x}, t)$ acting, respectively, on the fiber and fluid at the boundary nodes $\mathbf{x} \in \Gamma$ at time t . According to Newton's third law, $\mathbf{F}_{f_{si}}(\mathbf{x}, t) = -\mathbf{g}(\mathbf{x}, t)$ for $\mathbf{x} \in \Gamma$. The motion of the fluid governed by the Navier-Stokes and continuity equations with the inclusion of the external boundary force is written as

$$\begin{cases} \rho \frac{\partial \mathbf{u}}{\partial t} + \rho \mathbf{u} \cdot \nabla \mathbf{u} = -\nabla p + \mu \nabla^2 \mathbf{u} + \mathbf{g}(\mathbf{x}, t) \\ \nabla \cdot \mathbf{u} = 0 \end{cases} \quad (\text{A1})$$

$$\text{where } \mathbf{g}(\mathbf{x}, t) = \begin{cases} -\mathbf{F}_{f_{si}}(\mathbf{x}, t) & \text{if } \mathbf{x} \in \Gamma \\ 0 & \text{if } \mathbf{x} \notin \Gamma \end{cases} \quad (\text{A2})$$

The solid-fluid interaction force per unit volume acting on the solid boundary node is given by

$$\mathbf{F}^{f_{si}}(\mathbf{x}_s, t) = \frac{\rho_f [\mathbf{V}_f(\mathbf{x}_s, t) - \mathbf{V}_s(\mathbf{x}_s, t - \Delta t^{\text{LBM}})]}{\Delta t^{\text{LBM}}}, \quad \mathbf{x}_s \in \Gamma_s, \quad (\text{A3})$$

where the LBM time step $\Delta t^{\text{LBM}} = 1$, $\mathbf{V}_s(\mathbf{x}_s, t - \Delta t^{\text{LBM}})$ is the particle velocity at solid boundary node \mathbf{x}_s at the previous time step, and $\mathbf{V}_f(\mathbf{x}_s, t)$ is the fluid velocity at solid boundary node \mathbf{x}_s at time t :

$$\mathbf{V}_f(\mathbf{x}_s, t) = \int_{\Gamma_f} \mathbf{u}(\mathbf{x}_f, t) D(\mathbf{x}_f - \mathbf{x}_s) d\mathbf{x}_f, \quad \mathbf{x}_s \in \Gamma_s, \mathbf{x}_f \in \Gamma_f, \quad (\text{A4})$$

where $D(\mathbf{x}_f - \mathbf{x}_s)$ is a discrete Dirac delta function [24]. The feedback force on the fluid boundary nodes (Γ_f) is given by

$$\mathbf{g}(\mathbf{x}_f, t) = - \int_{\Gamma_s} \mathbf{F}^{f_{si}}(\mathbf{x}_s, t) D(\mathbf{x}_f - \mathbf{x}_s) d\mathbf{x}_s, \quad \mathbf{x}_s \in \Gamma_s, \mathbf{x}_f \in \Gamma_f. \quad (\text{A5})$$

A total force $\mathbf{F}(\mathbf{x}_s^i, t)$ acting on a node i of the solid object is the combination of the fluid-solid interaction force $\mathbf{F}^{f_{si}}(\mathbf{x}_s, t)$ at this node and the external force $\mathbf{F}^{\text{ext}}(\mathbf{x}_s, t)$ which could include the gravitational force and interparticle contact forces. For a particle with N boundary nodes, the total force $\mathbf{F}(t)$ and the torque $\mathbf{T}(t)$ at time t are given by

$$\mathbf{F}(t) = \sum_{i=1}^N \mathbf{F}(\mathbf{x}_s^i, t), \quad (\text{A6})$$

and

$$\mathbf{T}(t) = \sum_{i=1}^N (\mathbf{x}_s^i - \mathbf{x}_s^c) \times \mathbf{F}(\mathbf{x}_s^i, t), \quad (\text{A7})$$

respectively, where \mathbf{x}_s^c is the center of gravity of the particle. Once the total force and torque are obtained for each particle, the velocity and angular velocity of the suspending particle can be computed numerically by the Newtonian dynamics equations

$$\begin{cases} M \frac{d\mathbf{V}}{dt} = \mathbf{F}(t) \\ \mathbf{I} \frac{d\boldsymbol{\Omega}}{dt} + \boldsymbol{\Omega} \times (\mathbf{I} \cdot \boldsymbol{\Omega}) = \mathbf{T}(t) \end{cases} \quad (\text{A8})$$

where M and \mathbf{I} are the mass and the inertial tensor of the particle, respectively.

APPENDIX B: INTERPARTICLE MODEL

The applied lubrication force model between fiber-fiber and fiber-wall is based on a distance h and a relative velocity \mathbf{V}_{app} between the surfaces [19]

$$\mathbf{F}_{\text{lub}} = \begin{cases} -\frac{3\bar{q}\mu r}{2\sigma_c^2} \left(\frac{1}{h^2} - \frac{1}{\sigma_c^2} \right) \mathbf{V}_{\text{app}} \cdot \mathbf{n}_{\text{avg}}, & \text{if } h < \sigma_c \\ 0, & \text{if } h \geq \sigma_c \end{cases} \quad (\text{B1})$$

$$\mathbf{n}_{\text{avg}} = \frac{\mathbf{n}_i - \mathbf{n}_j}{|\mathbf{n}_i - \mathbf{n}_j|}, \quad (\text{B2})$$

$$\mathbf{V}_{\text{app}} = (\mathbf{V}_i - \mathbf{V}_j) \cdot \mathbf{n}_{\text{avg}}, \quad (\text{B3})$$

where, \bar{q} is a weighting factor that depends on the lattice structure, with $\bar{q} = 0.6$ for the D3Q19 lattice used in this paper. r is the fiber radius, \mathbf{n}_{avg} is the average surface normal vector between two surfaces i and j , and \mathbf{V}_i and \mathbf{V}_j are the velocities at the respective surface. To avoid the singular nature of h^{-2} term in the lubrication force model, we use a repulsive force when h is smaller than a critical distance, σ_c . The repulsive force increases exponentially with fiber surface overlap to prevent fibers from penetrating each other,

$$\mathbf{F}_{\text{con}} = A_c \exp\left(\frac{\sigma_c - h}{\sigma_c}\right). \quad (\text{B4})$$

Here A_c is a contact scaling constant, and σ_c is a constant determining the range of the contact force. In this paper $\sigma_c = 0.03r$ is chosen. The contact scaling is related to a viscous force as, $A_c \sim 6\pi\mu V_s/r$, where $V_s = |\mathbf{V}_{\text{app}}|$ is the relative velocity between the fibers.

APPENDIX C: LATTICE BOLTZMANN METHOD WITH AN EXTERNAL FORCE

The governing equation for the single distribution function $f(\mathbf{x}, \boldsymbol{\xi}, t)$ discretized in space \mathbf{x} , in lattice velocity $\boldsymbol{\xi}$, and in time t , is the Boltzmann equation,

$$\frac{\partial f}{\partial t} + \boldsymbol{\xi} \cdot \nabla_{\mathbf{x}} f + \mathbf{g} \cdot \nabla_{\boldsymbol{\xi}} f = J(f), \quad (\text{C1})$$

where \mathbf{g} is an acceleration related to forces acting on the particle; $J(f)$ is a collision operator. The original Boltzmann collision operator is extremely complex and is generally replaced by a simpler form. The simplest and most common model for $J(f)$ is the BGK approximation [33,34]. It is a linear relaxation-type model in which the current single particle distribution f is relaxed toward its equilibrium distribution f^{eq} ,

$$\frac{\partial f}{\partial t} + \boldsymbol{\xi} \cdot \nabla_{\mathbf{x}} f + \mathbf{g} \cdot \nabla_{\boldsymbol{\xi}} f = \frac{1}{\tau} (f^{\text{eq}} - f), \quad (\text{C2})$$

where τ is the relaxation time. Under appropriate lattice discretization of space \mathbf{x} and velocity $\boldsymbol{\xi}$, the simplest algorithm

to solve Eq. (C2) in discretized space is [35]

$$f_{\alpha}(\mathbf{x} + \mathbf{e}_{\alpha} \delta_t, t + \delta_t) - f_{\alpha}(\mathbf{x}, t) = -\frac{f_{\alpha}(\mathbf{x}, t) - f_{\alpha}^{\text{eq}}(\mathbf{x}, t)}{\hat{\tau}} + \frac{\delta_t^2}{\hat{\tau} \delta_x} \frac{\mathbf{g} \cdot (\mathbf{e}_{\alpha} - \mathbf{u})}{2c_s^2} f_{\alpha}(\mathbf{x}, t) \quad (\text{C3})$$

where $\hat{\tau}$ is the dimensionless relaxation time related to the kinematic fluid viscosity,

$$\nu = \delta_i c_s^2 \left(\hat{\tau} - \frac{1}{2} \right), \quad (\text{C4})$$

where δ_x and δ_t are the step of spatial discretization and step size in time, respectively, c_s is the pseudospeed of sound, and it is related to the temperature as $c_s = \sqrt{RT}$. The distribution function f can be used to determine the macroscopic hydrodynamics using the following relations:

$$\rho(\mathbf{x}, t) = \sum_{\alpha=1}^Q f_{\alpha}; \quad \rho \mathbf{u}(\mathbf{x}, t) = \sum_{\alpha=1}^Q f_{\alpha} \mathbf{e}_{\alpha}, \quad (\text{C5})$$

where ρ is the dimensionless density and \mathbf{u} is the dimensionless velocity of the fluid. The equilibrium distribution function at \mathbf{x} at time t reads

$$f_{\alpha}^{\text{eq}} = w_{\alpha} \rho \left\{ 1 + \frac{\mathbf{e}_{\alpha} \cdot \mathbf{u}}{c_s^2} + \frac{1}{2} \frac{(\mathbf{e}_{\alpha} \cdot \mathbf{u})^2}{c_s^4} - \frac{1}{2} \frac{\mathbf{u} \cdot \mathbf{u}}{c_s^2} \right\} + O(\mathbf{u}^3), \quad (\text{C6})$$

where w_{α} is a set of directional weights normalized to unity. For lattice type used in this paper (D3Q19), $w_0 = 2/9$, $w_{\alpha} = 1/9$ for $\alpha = 1, \dots, 6$ and $w_{\alpha} = 1/72$ for $\alpha = 7, \dots, 14$ and $Q = 19$.

APPENDIX D: ENTROPIC LATTICE BOLTZMANN METHOD

The entropic lattice Boltzmann method (ELB) introduces a self-adaptive stabilization by choosing automatically the over-relaxation γ at each node, which guarantees the distribution function f_{α} to be positive-definite at all locations and all discrete time steps. A form of the ELB approach is given by Keating *et al.* [21] and Ansumali *et al.* [36], as a modification of Eq. (C3),

$$f_{\alpha}(\mathbf{x} + \mathbf{e}_{\alpha}, t + 1) - f_{\alpha}(\mathbf{x}, t) = -\frac{\gamma(\mathbf{x}, t)}{2\hat{\tau}} \{ f_{\alpha}(\mathbf{x}, t) - f_{\alpha}^{\text{eq}}(\mathbf{x}, t) \}. \quad (\text{D1})$$

Here $\gamma(\mathbf{x}, t)$ is the maximal over-relaxation, which is the positive root of the entropy condition

$$H[\mathbf{f}] = H[\mathbf{f} - \gamma(\mathbf{f} - \mathbf{f}^{\text{eq}})]. \quad (\text{D2})$$

The discrete H function is derived upon applying Gauss-Hermite quadratures on the standard continuum Boltzmann H function, yielding

$$H[f_{\alpha}] = \sum_{\alpha=1}^Q f_{\alpha} \ln \left(\frac{f_{\alpha}}{w_{\alpha}} \right). \quad (\text{D3})$$

The effective viscosity in the Navier-Stokes equation for the ELB is

$$\nu_{\text{eff}}(\mathbf{x}, t) = \delta_i c_s^2 \left[\frac{2\hat{\tau}}{\gamma(\mathbf{x}, t)} - \frac{1}{2} \right]. \quad (\text{D4})$$

- [1] F. Lundell, L. D. Söderberg, and P. H. Alfredsson, *Annu. Rev. Fluid Mech.* **43**, 195 (2011).
- [2] G. B. Jeffery, *Proc. R. Soc. A* **102**, 161 (1922).
- [3] Z. Yu, N. Phan-Thien, and R. I. Tanner, *Phys. Rev. E* **76**, 026310 (2007).
- [4] H. Altenbach, I. Brigadnov, and K. Naumenko, *Zamm-Z. Angew. Math. Mech.* **89**, 823 (2009).
- [5] F. Lundell, *Phys. Fluids* **23**, 011704 (2011).
- [6] R. Larson and H. Öttinger, *Macromolecules* **24**, 6270 (1991).
- [7] P. Krochak, J. Olson, and D. Martinez, *J. Fluid Mech.* **653**, 431 (2010).
- [8] H. Zhang, G. Ahmadi, F. Fan, and J. McLaughlin, *Int. J. Multiphase Flow* **27**, 971 (2001).
- [9] P. H. Mortensen, H. I. Andersson, J. Gillissen, and B. J. Boersma, *Phys. Fluids* **20**, 093302 (2008).
- [10] C. Marchioli, M. Fantoni, and A. Soldati, *Phys. Fluids* **22**, 033301 (2010).
- [11] J. Paschkewitz, Y. Dubief, C. Dimitropoulos, E. Shaqfeh, and P. Moin, *J. Fluid Mech.* **518**, 281 (2004).
- [12] R. Benzi, E. S. C. Ching, E. De Angelis, and I. Procaccia, *Phys. Rev. E* **77**, 046309 (2008).
- [13] J. Gillissen, B. J. Boersma, P. H. Mortensen, and H. I. Andersson, *J. Fluid Mech.* **602**, 209 (2008).
- [14] H. Andersson, L. Zhao, and M. Barri, *J. Fluid Mech.* **696**, 319 (2012).
- [15] M. Kvik, Håkansson, F. K. Lundell, L. Prah Wittberg, and L. Söderberg, Licentiate thesis, Royal Institute of Technology (KTH), Stockholm, Sweden, 2012.
- [16] A. Ten Cate, J. Derksen, L. Portela, and H. Van Den Akker, *J. Fluid Mech.* **519**, 233 (2004).
- [17] M. Uhlmann, *Phys. Fluids* **20**, 053305 (2008).
- [18] M.-G. Villalba, A. G. Kidanemariam, and M. Uhlmann, *Int. J. Multiphase Flow* **46**, 54 (2012).
- [19] C. Aidun and J. Clausen, *Annu. Rev. Fluid Mech.* **42**, 439 (2010).
- [20] F. Janoschek, F. Toschi, and J. Harting, *Phys. Rev. E* **82**, 056710 (2010).
- [21] B. Keating, G. Vahala, J. Yopez, M. Soe, and L. Vahala, *Phys. Rev. E* **75**, 036712 (2007).
- [22] J. Wu and C. Aidun, *Int. J. Multiphase Flow* **36**, 202 (2010).
- [23] J. Wu and C. Aidun, *Int. J. Numer. Meth.* **62**, 765 (2010).
- [24] C. Peskin, *Acta Numer.* **11**, 479 (2003).
- [25] C. Schmid, L. Switzer, and D. Klingenberg, *J. Rheol.* **44**, 781 (2000).
- [26] S. Lindström and T. Uesaka, *Phys. Fluids* **19**, 113307 (2007).
- [27] R. Cox, *J. Fluid Mech.* **45**, 625 (1971).
- [28] M. Chevalier, P. Schlatter, A. Lundbladh, and D. Henningson, Tech. Rep. TRITA-MEK 2007:07, KTH Mechanics, Stockholm, Sweden (2007).
- [29] J. Jiménez and P. Moin, *J. Fluid Mech.* **225**, 213 (1991).
- [30] R. Moser, J. Kim, and N. Mansour, *Phys. Fluids* **11**, 943 (1999).
- [31] P. H. Mortensen, H. I. Andersson, J. Gillissen, and B. J. Boersma, *Int. J. Multiphase Flow* **34**, 678 (2008).
- [32] T. Rosén, F. Lundell, M. Do-Quang, and C. K. Aidun, in *8th International Conference on Multiphase Flow (ICMF)*, Jeju, South Korea, 2013.
- [33] H. Chen, S. Chen, and W. H. Matthaeus, *Phys. Rev. A* **45**, R5339 (1992).
- [34] S. Chen and G. Doolen, *Annu. Rev. Fluid Mech.* **30**, 329 (1998).
- [35] R. Nourgaliev, T. Dinh, T. Theofanous, and D. Joseph, *Int. J. Multiphase Flow* **29**, 117 (2003).
- [36] S. Ansumali, I. V. Karlin, and H. C. Öttinger, *Europhys. Lett.* **63**, 798 (2003).